DOI: 10.37190/ABB-02488-2024-05

Finite Element Analysis of Double Diamond Lattice Structured Lumbar Interbody Fusion Cage with Different Biomaterials

D. Athikesavan[1*], M.S. Alphin[1], S. Meganathan[1]

[1]Department of Mechanical Engineering, Sri Sivasubramaniya Nadar College of Engineering, Kalavakkam, Chennai, Tamil Nadu, India

[*]Corresponding author: D. Athikesavan, Department of Mechanical Engineering, Sri Sivasubramaniya Nadar College of Engineering, Kalavakkam, Chennai, Tamil Nadu, India, e-mail address: d.athikesavan@gmail.com

Submitted: 24th July 2024

Accepted: 28th October 2024

Abstract

Purpose: In recent years, low back pain has emerged as a significant global health issue, largely attributed to the prevalence of lumbar disc degeneration (LDD). This increases high demand on implant manufacturing due to the uniqueness of each patient's anthropometry. Which creates a surge in the implant design and its performance study. This work employed finite element analysis to evaluate the efficacy of Interbody cage fusion in combination with different biostructures and biomaterials.

Methods: The Lumbar Model was created by incorporating a surgical implant cage that featured three different lattice architectures using Boolean operations. We constructed four models, one model that was not altered and three models that underwent surgical procedures. The surgical models consist of three types of lattice implants are Double Diamond (DD), Double Diamond Centre Support (DDCS), Double Diamond Side Support (DDSS).

Results: The results indicate that the Double Diamond (DD) lattice-structured polyether ether ketone (PEEK) material implant experiences the most deformation, measuring 0.67 mm, when subjected to axial rotation motion. An analysis indicates the implant made with the DDCS lattice structure and Ti-6Al-4V material is subjected to the least stress – it stood at 75.47 MPa as the smallest stress level recorded.

Conclusion: The result of endplate von mises stress shows the PEEK material with DDCS lattice structured implant have low stress. Ti-6Al-4V and Stainless steel having high stress of 20 MPa on endplates. Comparatively Ti-6Al-4V having very good response with literature data. These results are providing insights towards the selection of implant in future medical treatment.

Keywords

Biomaterial, Biostructure, Lumbar, Von Mises Stress, Lattice Structure, Implant.

1. INTRODUCTION

One of the leading causes of low back pain, which often begins around age 20, is the degeneration of the intervertebral discs, which accelerates quickly after age 40 [33]. As these discs degenerate, height is lost, and pain is felt locally. If left untreated, this pain may worsen and develop

into nerve issues. Neural tissue may become constricted and narrow with continued ageing, which can result in spinal stenosis, a major cause of the great distress experienced by the elderly [27].

Degenerative processes cause structural damage to the intervertebral disc, specifically to its central nucleus pulposus, reducing flexibility. Herniation is a result of decreasing height and increasing pressure the degenerating process causes the disc's water content to be lost which reduces the disc's elasticity when subjected to mechanical pressure [41].

Proteoglycan loss alone deteriorates disc movement because serum proteins and cytokines permeate the disc and directly affect the cells hastening their degeneration. As a result of this degeneration process the spine may eventually become weak in segments [6]. Interbody cages have always been produced using machine methods during posterior surgical interventions for spinal instability[26] however this process may have drawbacks when it comes to producing complex geometries.

However, due to their ability to create intricate structures several 3D printing techniques have become more and more popular in recent years. This enables the creation of personalized implants for patients that consider the anatomy of their spines including variances in spinal curvature such as kyphosis and lordosis, among other conditions [12],[32]. Treatment of spinal deformities has benefited from this technology's increased capacity for precision and customisation in implant design. The best cage model for the L1-L2 disc space was developed after investigating different lumbar interbody cage designs. Johnson et al. studied the model with lattice porosities of 10.64%, 14.05 %, and 17.94%. Through finite element analysis (FEA), the model with 14.05 % porosity showed the highest general rigidity and stress distribution. Their research on lattice hybrid spine cages using the finite element method (FEM) revealed that the best fatigue life and tension protection were obtained when pore sizes 0.6 mm [30]. Compared microporous and lattice designs in interbody cages, noting that lattice-structured titanium cages promoted bone growth and segmental stability within 12 weeks, while microporous cages did not affect stiffness [35].

Designed four units with specific beam diameters porosities and pore sizes using 3D printing to fabricate polymer lattice structures for interbody fusion cages [34]. With 50 percent porous unit cells pores measuring 0.6 mm and stiffness levels reaching 5 kN/mm these novel spinal cage designs demonstrated favourable properties for bone fusion. To reconstruct the upper cervical spine in a 12-year-old patient with C2 Ewing sarcoma we used 3D printing to create axial vertebral body

implants. After the staged spondylectomy the patient recovered more quickly than seven days thanks to the stabilized and optimized implants [30]. produced titanium prostheses using state-of-the-art 3D printing technology to treat a group of 13 patients' spinal tumours. In all patients there was subsidence into neighbouring vertebral bodies however in 11 of the 12 cases this was clinically insignificant [17].

One implant had to be removed because of a relapse of the disease and another patient needed revision surgery because the cage had collapsed. Likewise, Leary et al. used three-dimensional printing to treat a complicated primary spinal tumour [5]. In nine cases implants were used as reference models to help with intraoperative guidance and operation planning. Kuleshov and others. treated 52 patients with spinal deformities using 3D-printed models and all but three of them had stable spines as a result [39].

The current literature highlights a growing emphasis on studies related to 3D-printed interbody cages, especially concerning pore sizes and customized manufacturing, underscoring the relatively limited research on lattice structures. However, lattice-structured interbody cages demonstrate superior load transfer to vertebrae and a reduction in stress shielding [19]. This study aims to investigate the behaviour of fusion cages with varying lattice structures positioned between the L4 and L5 vertebrae through the application of finite element analysis. Additionally, the study improves the lattice structure of Ti6Al4V interbody cages through lattice topology optimization technology and verifies their static structure [13]. These findings offer new insights for future interbody fusion cage design.

2. MATERIALS AND MODELING

2.1. Significance of 3D printing in biostructure

3D printing revolutionizes medical implant technology by producing biostructures and intricate scaffolds that closely resemble tissues. These structures are critical for tissue engineering advancement and implant creation. Their internal design greatly influences their properties, which include a Double Diamond (DD) cube, a Double Diamond Centre Support (DDCS), a centre point,

and a Double Diamond Side Support (DDSS) cube with points on corners and faces. Various weight-bearing bones contain DDCS structures, which are known for their durability and stability. Supporting tissues encompass several structures that can maintain a delicate equilibrium between strength and flexibility. DDSS systems, which incorporate beams connecting interior areas, significantly enhance structural integrity. 3D printing facilitates the creation of biostructures with precise characteristics by altering internal designs, opening possibilities for enhanced medical implant therapies.

2.2. Creation of a Lumbar Finite Element Model

The FE lumbar model used in this current study has already been validated in previous research with literature and clinical data [20]. The process of the FE model is shown in Figure 1. The complete model previously utilised three lumbar vertebrae (L3–L5), [37]. The lumbar stability was enhanced by three surgical models that utilised various combinations of Coflex IPD and pedicle screws. This study utilized a consistent surgical lumbar model and examined three distinct implant lattice structures from three different biomaterials. Ti-6Al-4V, PEEK, and stainless steel (SS).

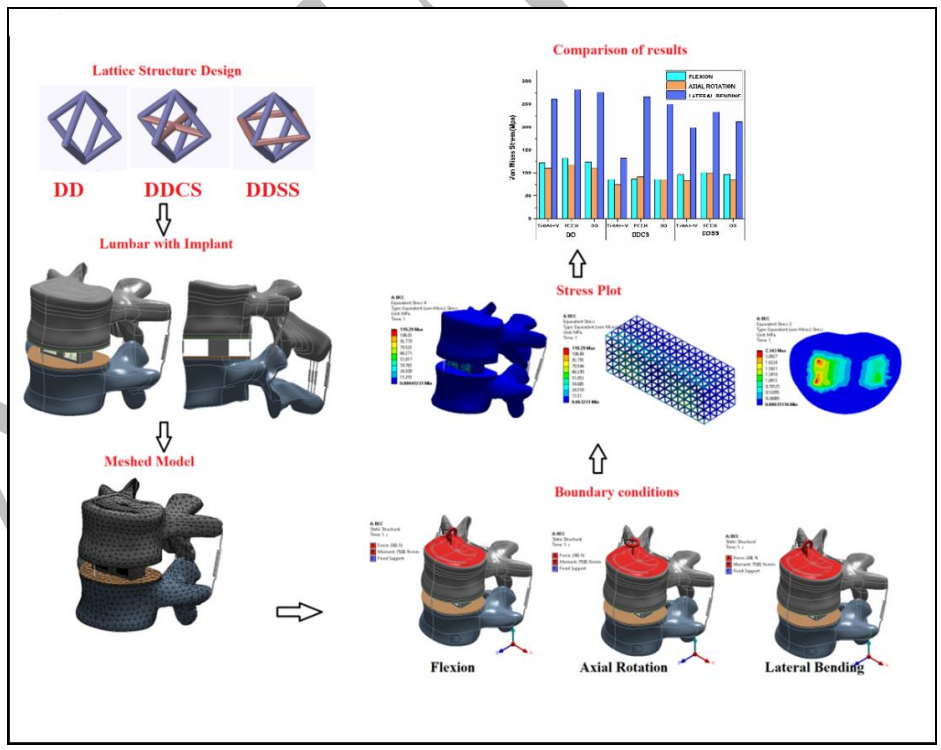

Fig. 1. Schematic flow diagram illustrating the step-by-step analytical technique.

The Lumbar Model was modified by incorporating a surgical implant cage that featured three different lattice architectures using Boolean operations. We constructed four models for our analysis. one model that was not altered and three models that underwent surgical procedures. The surgical models consist of three types of lattice implants. the Double Diamond (DD) lattice implant, the Double Diamond Centre Support (DDCS) lattice implant, and the Double Diamond Side Support (FDC) lattice implant.

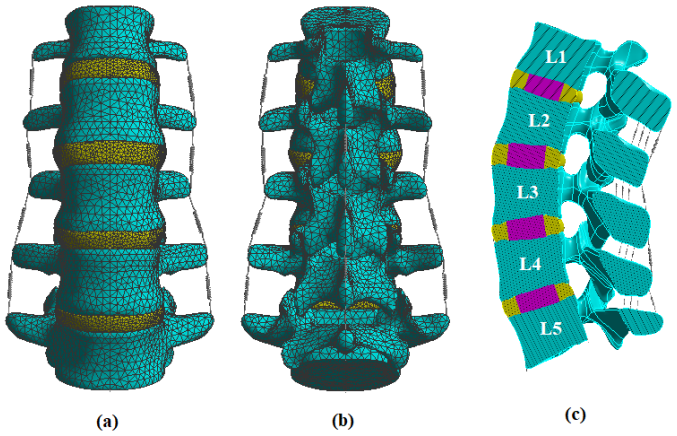

Fig. 2. (a) Anterior view of the Lumbar (L1-L5) FE model; (b) Posterior view of the Lumbar FE model; (c) Cross-sectional side view of the Lumbar FE model.

Table 1. Material properties of several components of the lumbar spine FE model and their corresponding values.

Part Name	**Young's Modulus Value (MPa)**	**Poisson Ratio**	**Cross Section Area (mm^2)**	**Density (Kg/mm^3)**	**References**
Cortical Bone	12,000	0.3	--	1.70×10^{-06}	[21]
Cancellous Bone	100	0.2	--	1.10×10^{-06}	[7]
Posterior Bone	3500	0.25	--	1.40×10^{-06}	
Endplate	24	0.25	--	1.20×10^{-06}	[2]

Annulus Fibrosus	4.2	0.45	--	1.05 x 10^{-06}	[10]
Anterior Longitudinal Ligament (ALL)	20	0.3	63.7	1.00 x 10^{-06}	
Posterior Longitudinal Ligament (PLL)	20	0.3	20	1.00 x 10^{-06}	[36] [40]
Ligament Flava (LF)	19.5	0.3	40	1.00 x 10^{-06}	[4]
Interspinal Ligament (ISL)	11.6	0.3	40	1.00 x 10^{-06}	
Supraspinal Ligament (SSL)	15	0.3	30	1.00 x 10^{-06}	
Intertransverse Ligament (ITL)	58.7	0.3	3.6	1.00 x 10^{-06}	
Ti-6Al-4V	113800	0.34	--	4.43 x 10^{-06}	
PEEK	3850	0.4	--	1.31 x 10^{-06}	
Stainless Steel	193000	0.31	--	7.75 x 10^{-06}	

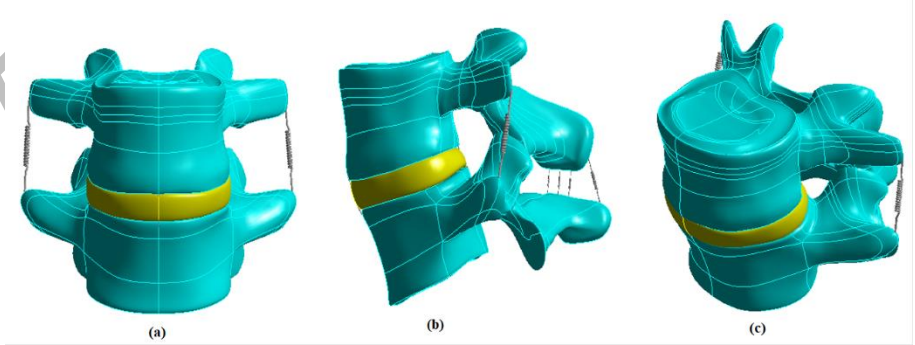

Fig. 3. (a) Front view of the reduced Lumbar (L4-L5) FE model; (b) Side view of the reduced Lumbar FE model; (c) Isometric view of the reduced Lumbar FE model.

This study primarily investigates the biomechanical reactions of the implant lattice structure on the L4-L5 vertebrae. To reduce the amount of time spent on computation, the range of L1-L5 is condensed to L4-L5 [38], as shown in Figure 3. Table 1 displays the material characteristics of the lumbar region. Ligaments are created by employing a spring unit that is subjected to tension stress only, and the stiffness of the ligament is determined by the attribute specified in Table 2.

Table 2. Ligament Stiffness in N-mm [8]

Ligaments	**ALL**	**PLL**	**ISL**	**SSL**	**LF**	**ITL**
L3-L4	40 ± 20	10.5 ± 8	18.1 ± 16	35 ± 11.7	35 ± 6.2	50
L4-L5	40.5 ± 14	25.8 ± 16	8.7 ± 6.5	18 ± 6.8	27.1 ± 12	50

2.3. Biostructure modelling for implants

The implant model was developed using unit cell modeling in Ansys Space Claim software. The unit cell is then developed by a solid model array algorithm, as shown in Figure 4. The unit cell size is 2 * 2 mm, followed by the implant developed with the following dimensions. 30 * 10*10 mm [9].

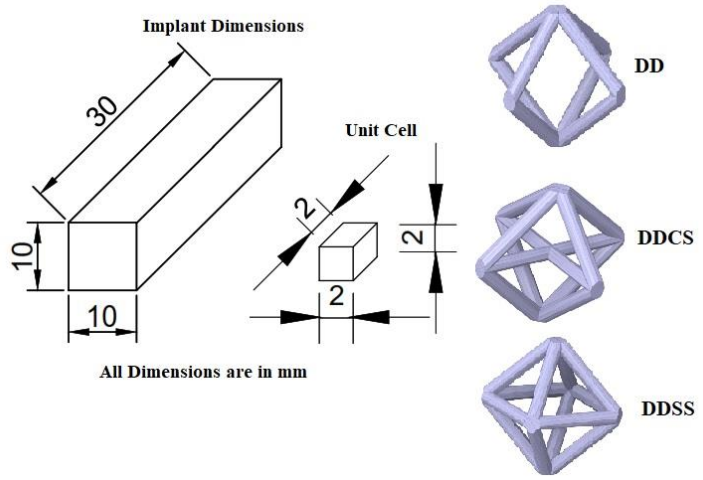

Fig. 4. Dimensions of Implant Design and Unit Cell

2.4. Materials and Mesh

The reduced Lumbar model was loaded into the Ansys workbench after the geometric adjustments. The initial step in the FE analysis procedure is to provide the parts with the requisite material properties. Tables 1 and 2 show the material properties of the lumbar spine [7],[15],[18],[21]. The material properties are based on data from several sources. Furthermore, the 59250 nodes and 35168 elements make up the 10 node tetrahedral components utilized to mesh the entire lumbar model (Figure 2). Furthermore, the surgical model with the implant consists of 423641 components and 895642 nodes [8],[29],[31]. The intervertebral and vertebral bodies create a fused union. The MPC contact creation algorithm is used to construct the contacts.

2.5. Boundary conditions

There are two parts to the current investigation. (1) validation of the intact finite element model; and (2) a surgical model with different lattice structured implant finite element analysis. The inferior surface of L5 in the Intact model is fixed. The Intact model applied four pure moments at 7.5 Nm. The superior surface of the L4 was then subjected to an axial compressive load of 1000 N. We confirmed that the lower surface of the L5 lumbar vertebra remained constant in the surgical models by utilizing the full degree of freedom fixed for the L5 inferior surface. The pure moments of 7.5 Nm in flexion (FL), lateral bending (LB), and axial rotation (AR) are the boundary conditions of the FE model located at the center of the L4 superior surface. Furthermore, a follower load of 280 N constituted half of the body weight along the lumbar spine curvature [14].

3.RESULTS

3.1. Validation of the Intact Model

The entire model L4-L5 was subjected to a pure moment of 7.5 Nm for four distinct motions. The range of motion (ROM) of the L4-L5, as determined for each specific movement, is illustrated in Figure 5(a). Furthermore, a 1000N axial load is applied to the upper surface of L4. The intradiscal pressure at the L4-L5 intervertebral disc (IVD4) was determined for four specific moments, as seen in Figure 5(b).

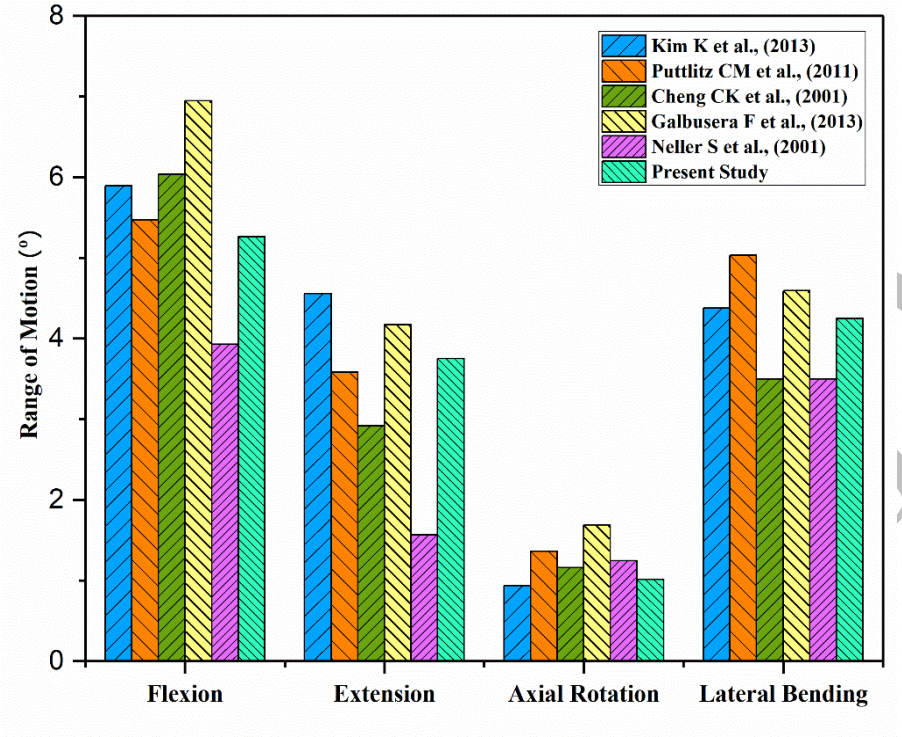

Fig. 5. (a). ROM of the Intact Model Comparison with Literature Data for Validation

The ROM comparison clearly demonstrates that the lumbar spine exhibits greater flexibility in flexion motion compared to all other pure moments. The projected results of the present investigation are mainly consistent with the data found in the literature [1],[3],[23],[25],[28]. The axial rotation has less flexibility compared to other types of motion. The comparison of intradiscal pressure in the fourth intervertebral disc (IVD 4) yields highly favorable results when compared to earlier research data. In general, the Intact reduced model (L4–L5) is reliable and valid.

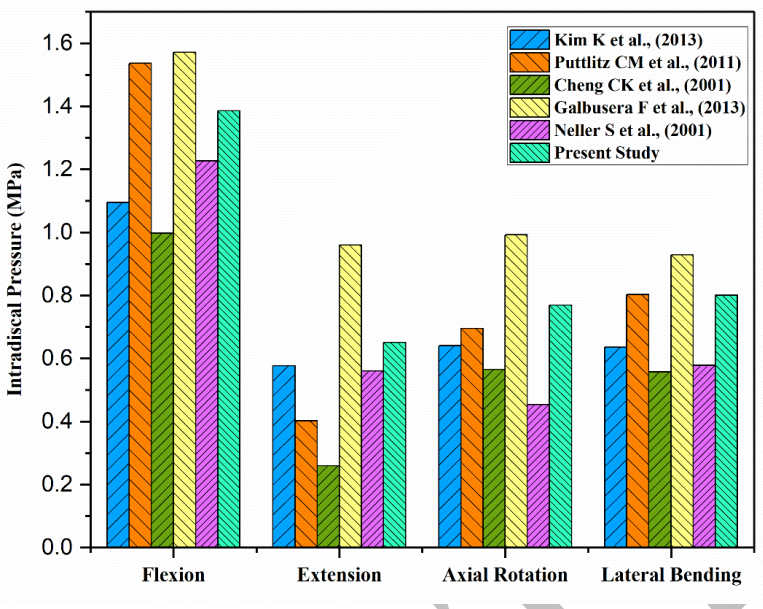

Fig. 5. (b). Intradiscal pressure of IVD4 compared with literature data for validation

3.2. Surgical Model Results

An analysis was performed utilizing finite element software to examine the L4-L5 spine and the implant with a lattice construction. The analysis entailed the application of force and moment. The analytical results comprised calculations for overall deformation and von Misses stress. The Double Diamond (DD) lattice structure PEEK material implant experiences a maximum spine deformation of 0.664 mm when subjected to lateral bending motion. Previous studies indicate that lateral bending is responsible for the highest magnitude of total deformation [9].

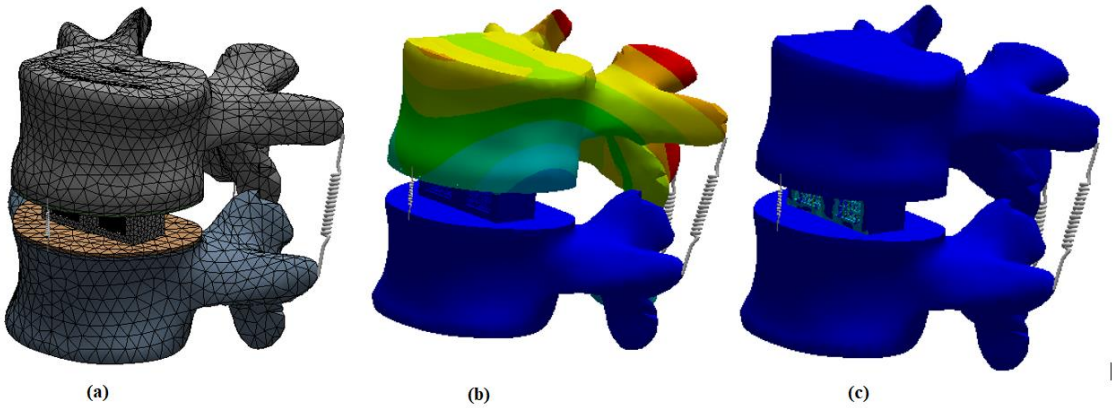

Fig. 6. (a) Preprocessed mesh view of L4-L5 with Implant; (b) Post processed result: Total Deformation; (c) Post processed result: Maximum von Mises Stress

The VMSS was calculated for a lumbar spine implant, which involved three different structures and combinations of materials. The Von Mises stress (VMS) was computed for both L4 and L5 lumbar end plates using several lattice-structured implants made of different biomaterials. The stress calculations were performed for three different motions, as depicted in Figure 6.

3.3. Calculation of Von Mises stress in the implant

The present study comprises three distinct lattice structures, namely DD, DDCS, and DDSS, fabricated from three different materials, including Ti-6Al-4V, PEEK, and stainless steel. These structures are subjected to three different types of motions. flexion, axial rotation, and lateral bending. The loading conditions consisted of an axial compression force of 280 N and a momentum of 7.5 Nm related to motion. Using the finite element analysis, a stress plot was generated for the implant, namely for the L4 and L5 endplates.

3.3.1 Double Diamond (DD) Lattice Structured Implant

The ongoing inquiry involves the examination of three distinct materials, namely Ti-6Al-4V, PEEK, and SS, subjected to three different types of motion. FL, AR, and LB. We conducted the investigation utilizing a DD lattice-structured implant, as depicted in Figure 7. The Von Misses stress graphs were created for the conditions. We compute a total of nine stress values for the implant. The minimum Von Misses stress recorded is 109.93 MPa in the case of AR with Ti-6Al-4V. Conversely, the maximum Von Misses stress observed is 282.98 MPa for LB with PEEK.

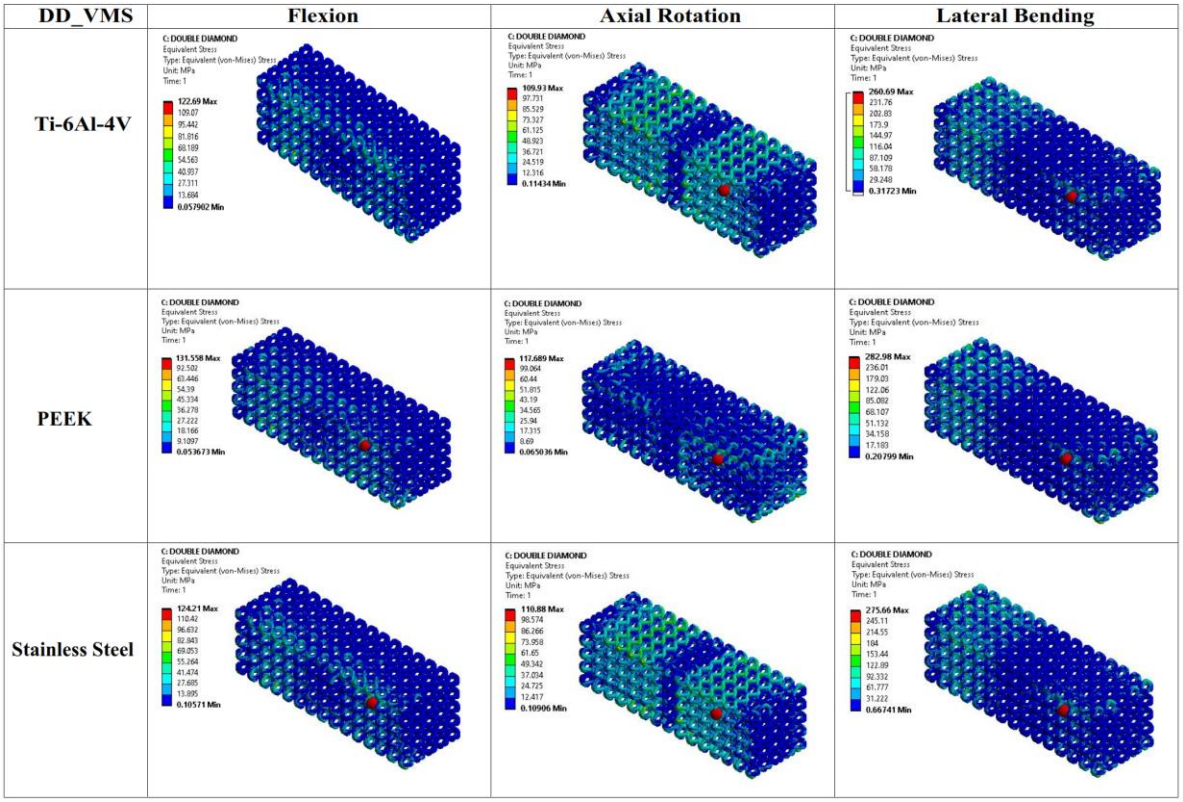

Fig. 7. Von Misses stress plot shows the relationship between the three distinct loading motions, biomaterial, and the implant DD lattice structure

3.3.2. Double Diamond Center Support (DDCS) Lattice Structured Implant

The current study uses three different materials, Ti-6Al-4V, PEEK, and SS, in three different motions. FL, AR, and LB. We ran the survey on a DDCS lattice-structured implant, as illustrated in Figure. 8.

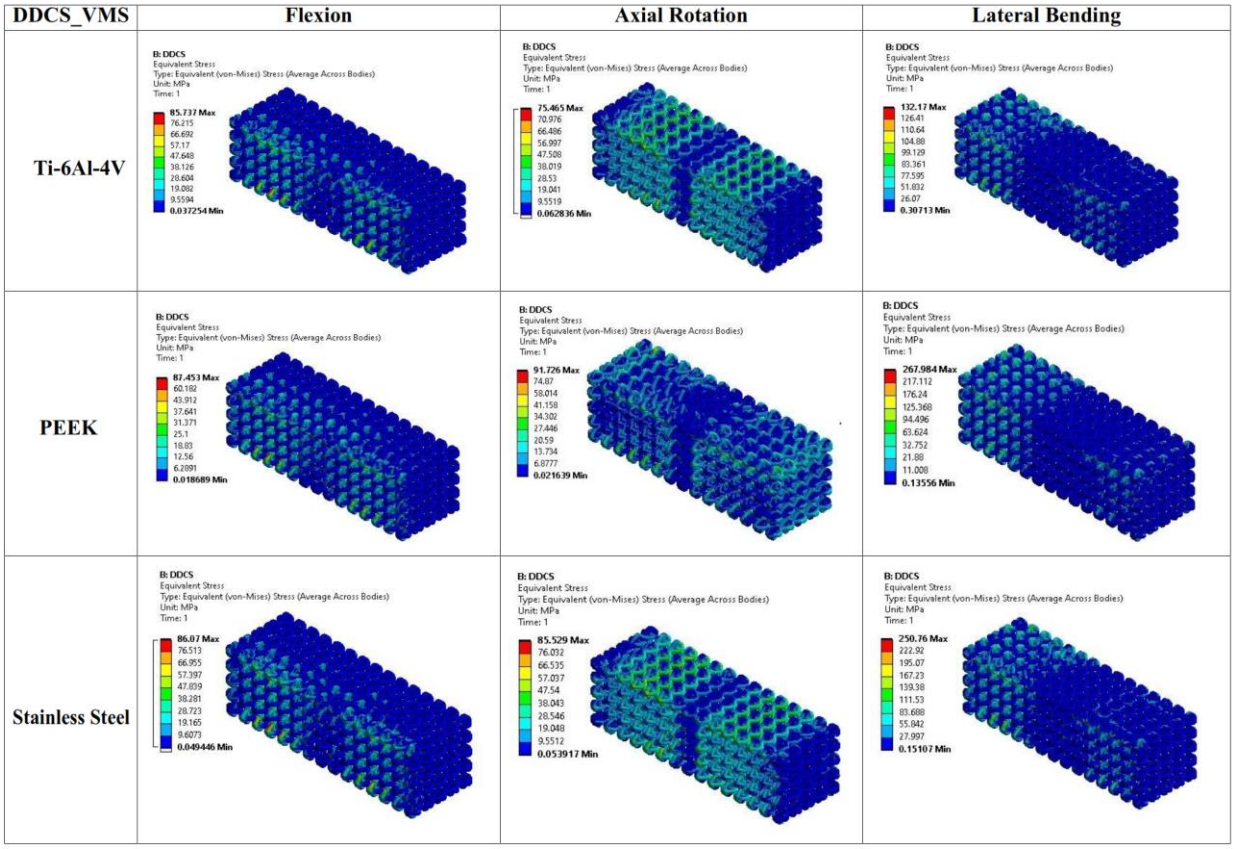

Fig. 8. Von Misses stress plot shows the relationship between the three distinct loading motions, biomaterial, and the implant DDCS lattice structure.

The Von Misses stress graphs were generated for the conditions. I computed a total of nine stress values for this structure. The minimum Von Misses stress recorded is 75.46 MPa in the case of AR with Ti-6Al-4V, whereas the maximum stress is 267.98 MPa observed in the LB with PEEK.

3.3.3. Double Diamond Side Support (DDSS) Lattice Structured Implant

The present work employs three distinct materials, namely Ti-6Al-4V, PEEK, and SS, in three distinct motions. FL, AR, and LB. An investigation was conducted on a lattice-structured implant called DDSS, as shown in Figure 9. The Von Misses stress graphs were generated based on the conditions. We calculated nine stress values. The minimum Von Misses stress recorded is 83.66 MPa, as seen in the FL specimen with Ti-6Al-4V material. Conversely, the maximum Von Misses stress is 234.30 MPa, found in the LB specimen with PEEK material.

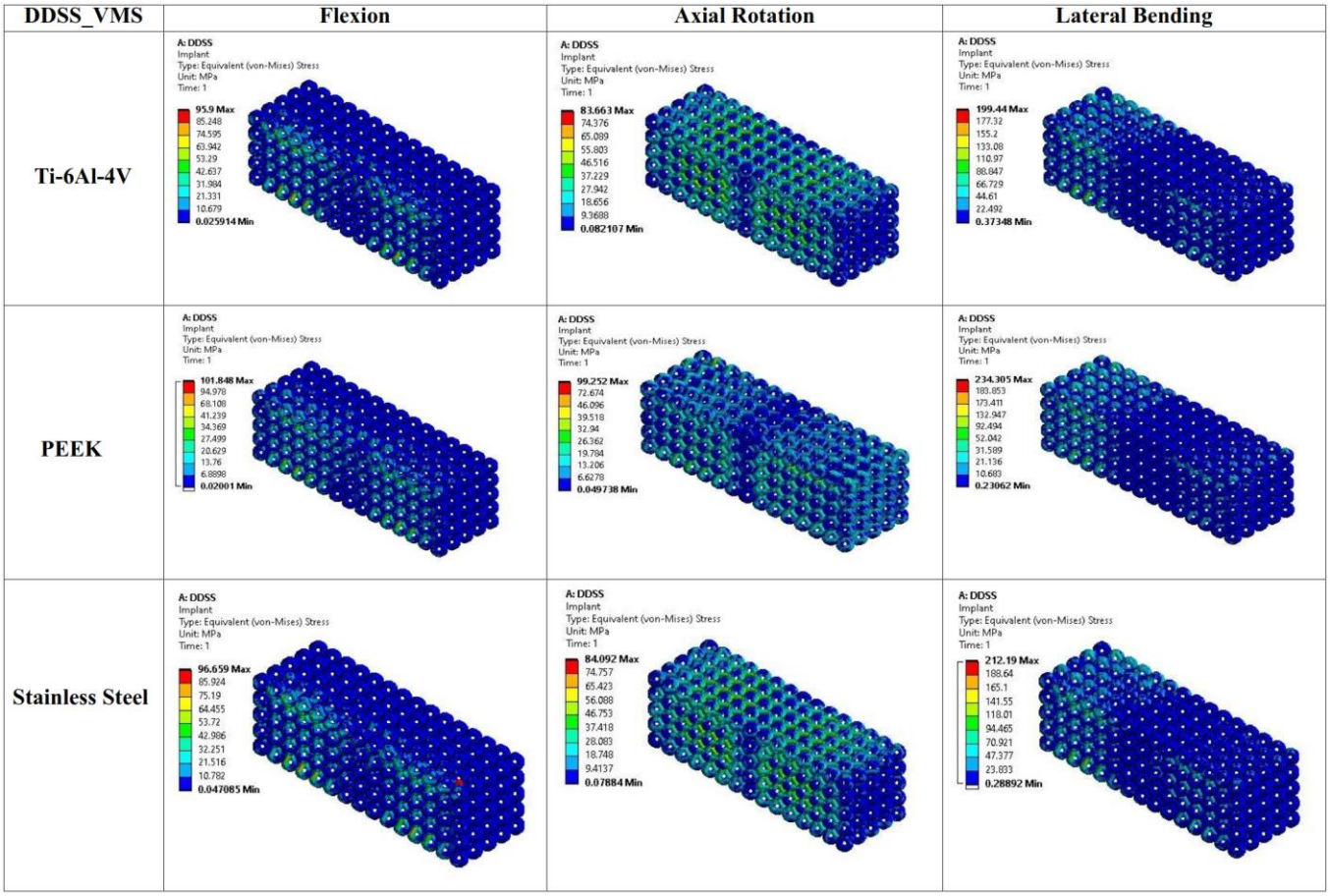

Fig. 9. Von Misses stress plot shows the relationship between the three distinct loading motions, biomaterial, and the implant DDSS lattice structure.

3.4. Calculation of Von Misses stress on the lumbar end plate

The endplates transfer the load between adjacent vertebrae. Individuals with osteoporosis or other bone diseases experience heightened deterioration of the end plates. This aids in determining the crucial loading conditions and precise placement of the lumbar region. For the biomechanical evaluation, we examined two lumbar endplates. The Von Misses stress of the L4 and L5 end plates is calculated. This study utilizes three different loads, materials, and a lattice-structured implant. A grand total of 27 stress plots were retrieved.

3.4.1. L4 end plate with Double Diamond Lattice Implant

The load is transferred from the lumbar (L4) to the implant through the L4 endplate. Figure 10 displays the Von Mises stress on the L4 end plate using a BCC lattice constructed implant. The investigation reveals that the minimum Von Misses stress is 11.23 MPa in the case of FL with PEEK, but the maximum stress reaches 19 MPa in the case of LB with Ti-6Al-4V.

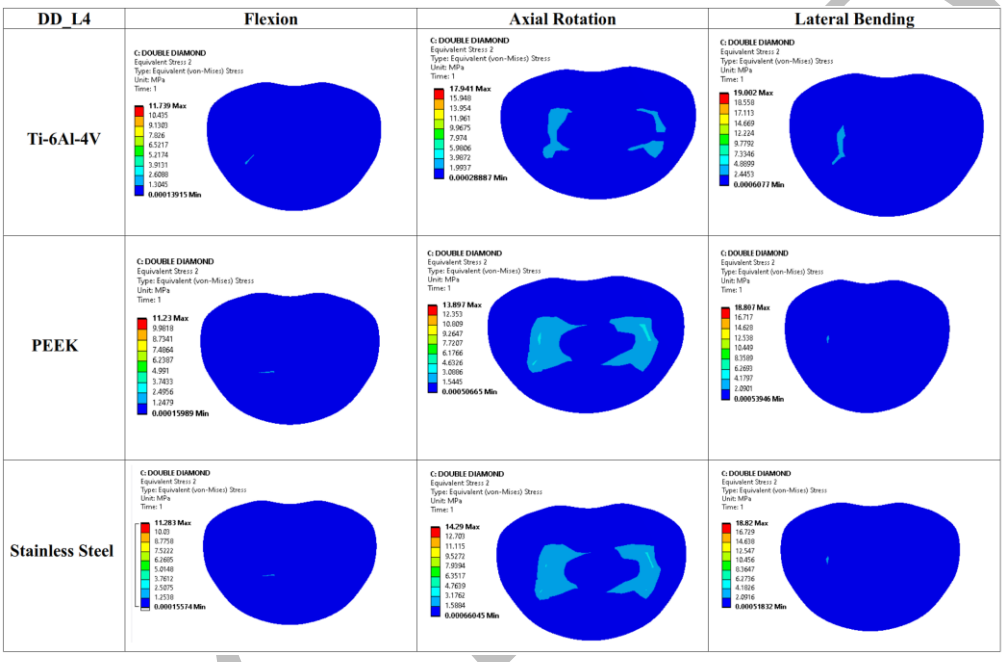

Fig. 10. Von Misses stress plot of the L4 end plate shows the relationship between the three distinct loading motions, biomaterial, and the implant DD lattice structure.

3.4.2. L4 end plate with Double Diamond Center Support (DDCS) Lattice Implant

Figure 11 displays the Von Mises stress on the L4 end plate using a lattice-structured implant known as DDCS. The research reveals that the lowest Von Misses stress is 9.24 MPa in the FL configuration with PEEK, whereas the highest stress is 14.42 MPa in the LB configuration with Ti-6Al-4V.

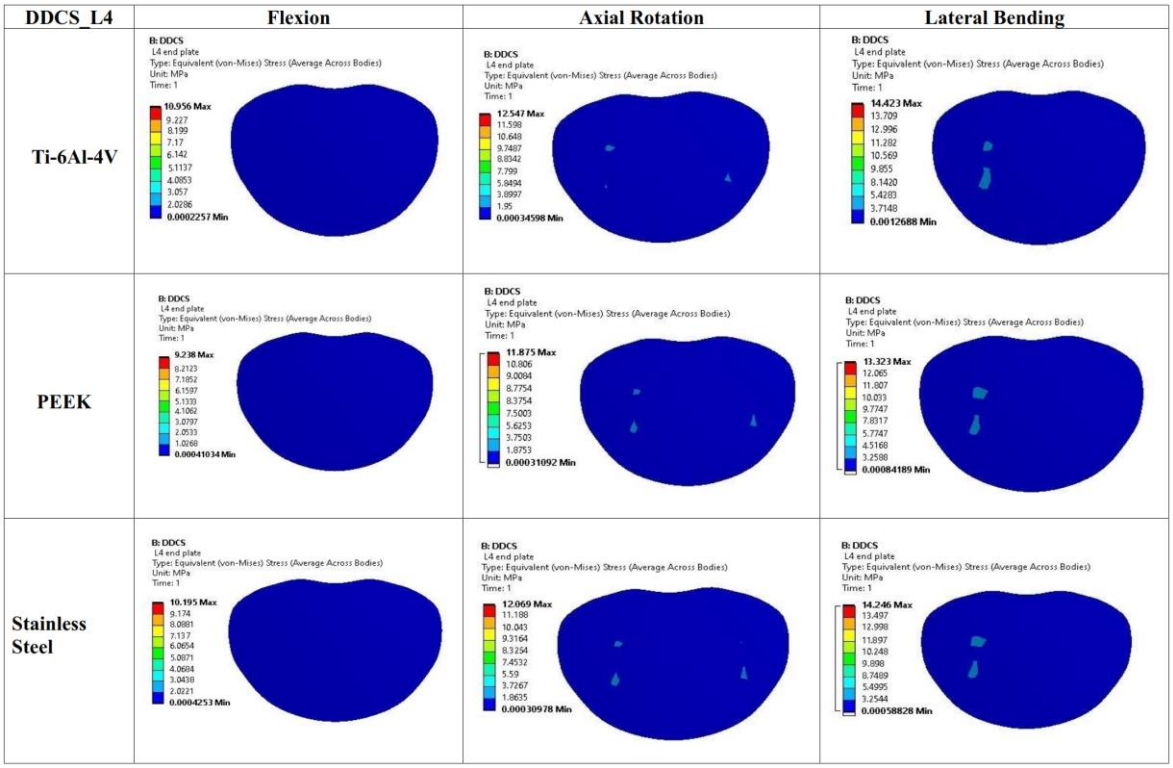

Fig. 11. Von Misses stress plot of the L4 end plate shows the relationship between the three distinct loading motions, biomaterial, and the implant DDCS lattice structure.

3.4.3. L4 end plate with Double Diamond Side Support (DDSS) Lattice Implant

Figure 12 displays the Von Mises stress at the L4 end plate using a lattice-structured implant called DDSS. The research reveals that the minimum Von Misses stress is 13.19 MPa, occurring in the AR with PEEK material. Conversely, the maximum Von Misses stress is 16.95 MPa, observed in the LB with Ti-6Al-4V material.

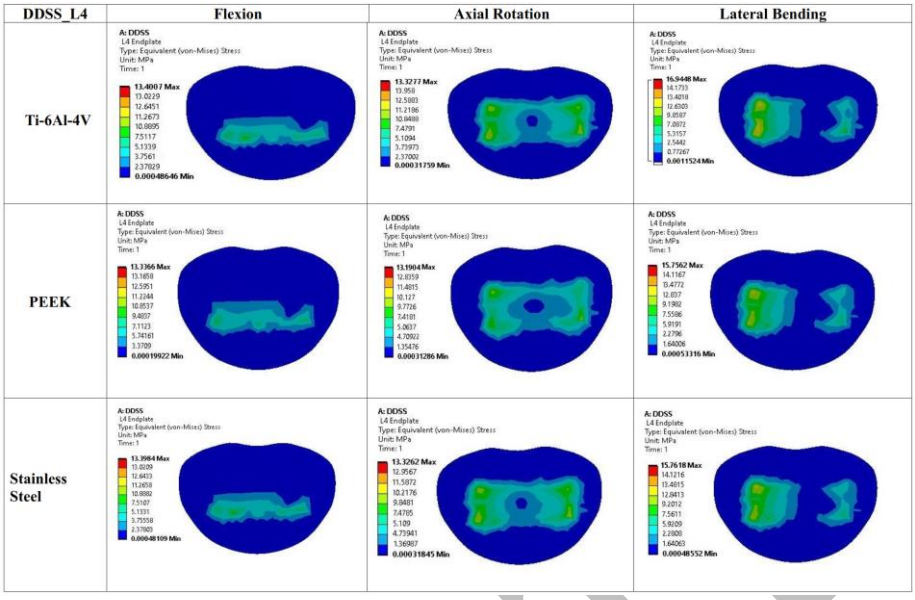

Fig. 12. Von Misses stress plot of the L4 end plate shows the relationship between the three distinct loading motions, biomaterial, and the implant DDSS lattice structure.

3.4.4. L5 end plate with double diamond lattice implant

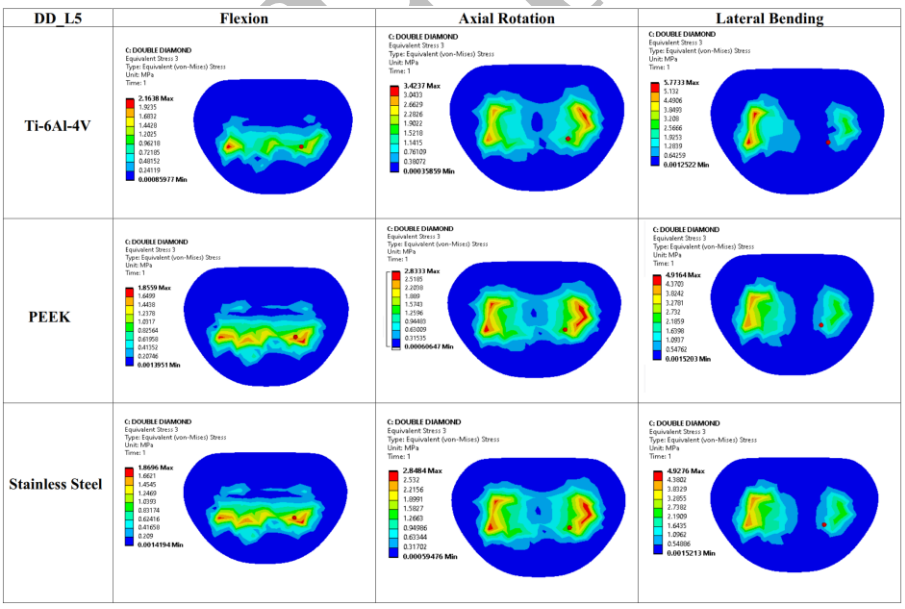

Fig. 13. Von Misses stress plot of the L5 end plate shows the relationship between the three distinct loading motions, biomaterial, and the implant DD lattice structure

Figure 13 displays the Von Mises stress at the L5 end plate using a Double Diamond lattice-structured implant. The research reveals that the minimum Von Misses stress is 1.86 MPa, occurring in the FL with PEEK material. Conversely, the greatest Von Misses stress is 5.77 MPa, observed in the LB with Ti-6Al-4V material.

3.4.5. L5 end plate with Double Diamond Center Support (DDCS) Lattice Implant

Figure 14 shows the L5 end plate Von Mises stress with an DDCS lattice-structured implant. In this analysis, the lowest Von Misses stress is 1.57 MPa (FL with PEEK), while the maximum is 4.31MPa (LB with Ti-6Al-4V).

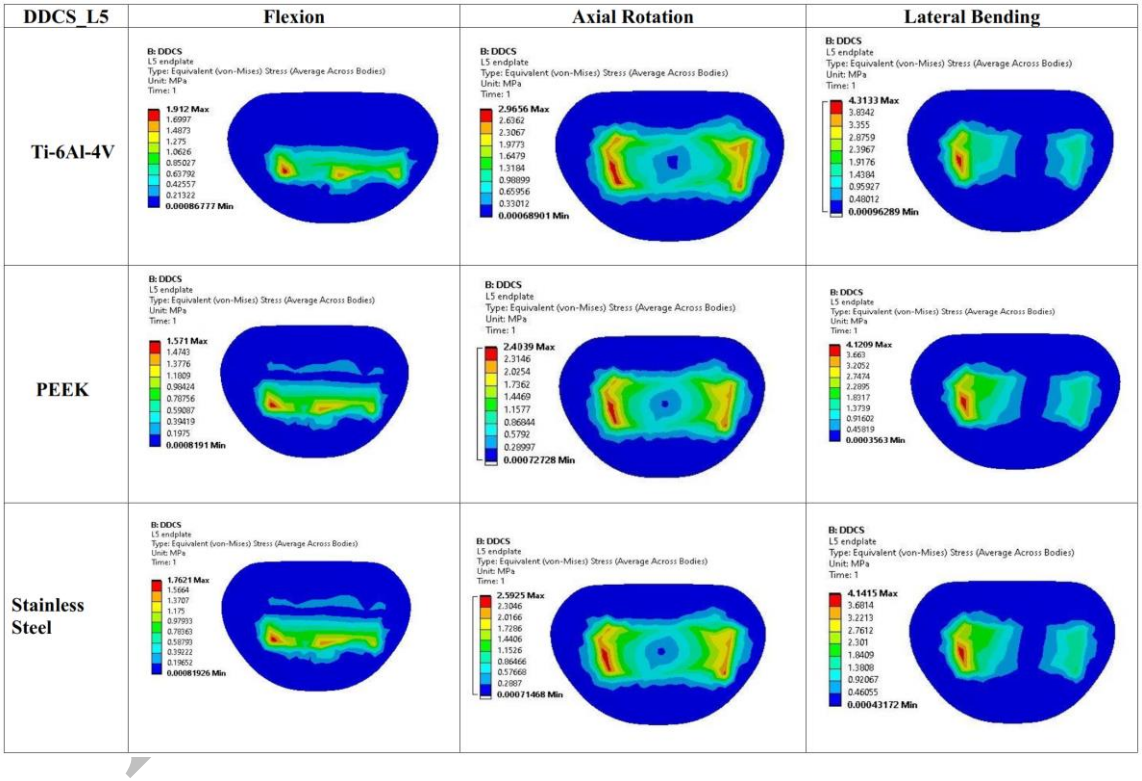

Fig. 14. Von Misses stress plot of the L5 end plate shows the relationship between the three distinct loading motions, biomaterial, and the implant DDCS lattice structure.

3.4.6. L5 end plate with Double Diamond Side Support Lattice Implant

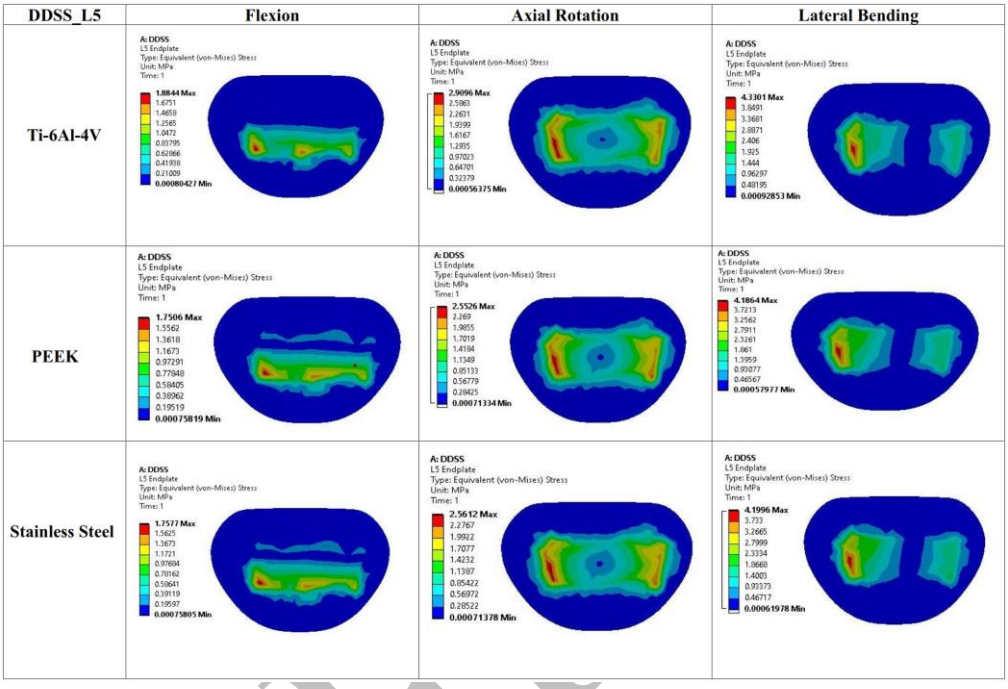

Fig. 15. Von Misses stress plot of the L5 end plate shows the relationship between the three distinct loading motions, biomaterial, and the implant DDSS lattice structure.

Figure 15 shows the L5 end plate Von Mises stress with an DDSS lattice-structured implant. In this analysis, the lowest Von Misses stress is 1.75 MPa (FL with PEEK), while the maximum is 4.33 MPa (LB with Ti-6Al-4V).

4. DISCUSSION

4.1. Numerical Validation

The design stress is validated against the material strength using analytical calculations.

General VMS equation for three dimensional problems

$$\sigma_v = \sqrt{\frac{1}{2}\left[(\sigma_{11} - \sigma_{22})^2 + (\sigma_{22} - \sigma_{33})^2 + (\sigma_{33} - \sigma_{11})^2\right] + 3(\tau_{12}^2 + \tau_{23}^2 + \tau_{31}^2)}$$

The VMS criterion is helpful for calculating the failure under complicated loading conditions such as bending, torsion, and combination loading for isotropic materials. To predict the failure or plastic deformation of the components under the combined loading condition, the Vms should be less than the material yield strength (σ_y).

$$\sigma_v < \sigma_y \text{ (Design Safe)}$$

In this study, we used three different materials. Ti-6Al-4V, stainless steel, and PEEK, which had the following yield strengths (σ_y) as shown in Table 3.

Table 3. Yield Strength of Implant material in N-mm

Material	**Yield Strength (Mpa)**	**Reference**
Ti-6Al-4V	1100	[8]
Stainless Steel	290	
PEEK	125	

4.2. Von Mises stress of an implant with a different lattice structure, material, and load

Designing lumbar implants poses numerous clinical challenges. Conventional implants have been noted to exhibit stress concentration in specific areas, leading to potential failures [16].

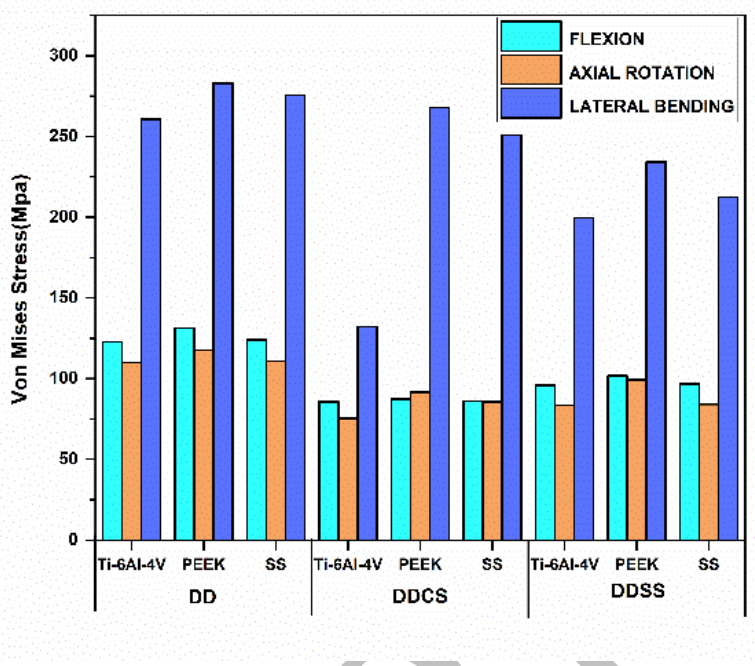

Fig. 16. Graphical representation of the VMS of an implant with a different lattice structure, material, and loading conditions.

Selecting the appropriate material for implants is crucial, involving evaluating factors such as mechanical strength, osseointegration, and the prevention of adverse reactions. Designing a universally applicable implant is challenging due to the inherent anatomical variations across patients and the limitations faced by surgeons when accessing the lumbar spine during surgery, highlighting the complexities of individual patient variability.

Lattice-structured implant is good in relation to loading conditions. These intricate, permeable designs resemble honeycombs and consist of interconnected components that create a lightweight structure [11]. By utilizing selective laser melting and other additive manufacturing techniques, personalized lattice patterns can be created for individual patients, effectively addressing the issue of patient variability. Figure 16 displays the von Mises stress of implants, including various lattice structures, materials, and loading conditions. It is evident that the Ti-6Al-4V material exhibits the lowest stress compared to all other materials. Furthermore, the analysis reveals that the DDCS structure exhibits the least amount of stress, measuring at 75.47 MPa, in comparison to the other structures. The highest stress value of 282.98 MPa occurs during lateral bending motion with

the DD structure. Literature reviews confirm that lateral bending is associated with maximum stresses.

4.3. Von Mises stress of the L4 endplate.

Finite Element Analysis (FEA) can provide insights into the biomechanics of the lumbar spine, namely by examining how stress is distributed across the surfaces that bear the essential load of the endplates, vertebrae, and discs. This crucial data enables clinicians to assess individualized therapies and interventions for patients [10].

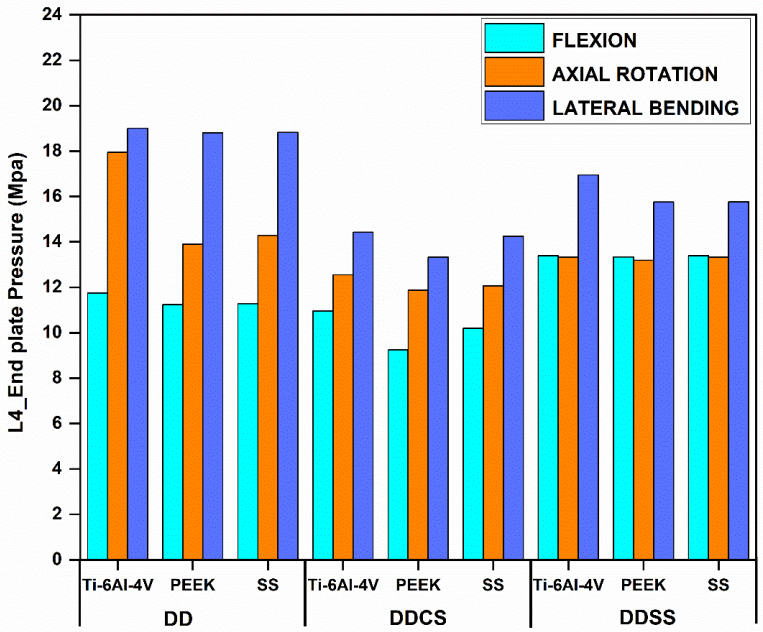

Fig. 17. Graphical representation of von Mises stress on the L4 endplate.

Figure 17 displays the von Mises stress of the L4 end plate under various lattice structured implants, materials, and loading conditions. These data clearly indicate that the PEEK material exhibits the lowest stress level (9.24 MPa) compared to all other materials. Furthermore, the analysis demonstrates that the DDCS structure exhibits the least amount of stress when compared to the other structures. The highest stress value of 19.00 MPa is observed during lateral bending motion with a DD structure with a Ti-6Al-4V material implant [1]. Literature reviews confirm that lateral bending is associated with the maximum stress at the end plate [11].

4.4. Von Mises stress of the L5 endplate.

Figure 18 displays the Von Mises stress (Vms) of the L5 end plate under various combinations of lattice structured implants, materials, and loading conditions. It is evident from this statement that the PEEK material has the least amount of stress compared to all other materials. Furthermore, the analysis reveals that the DDCS structure exhibits the lowest stress level of 1.57 MPa (FL with PEEK) in comparison to the other structures. The highest stress value of 5.77 MPa is observed during lateral bending motion with a DD structure with Ti-6Al-4V. Literature reviews indicate that lateral bending is associated with the maximum stress at the end plate [11].

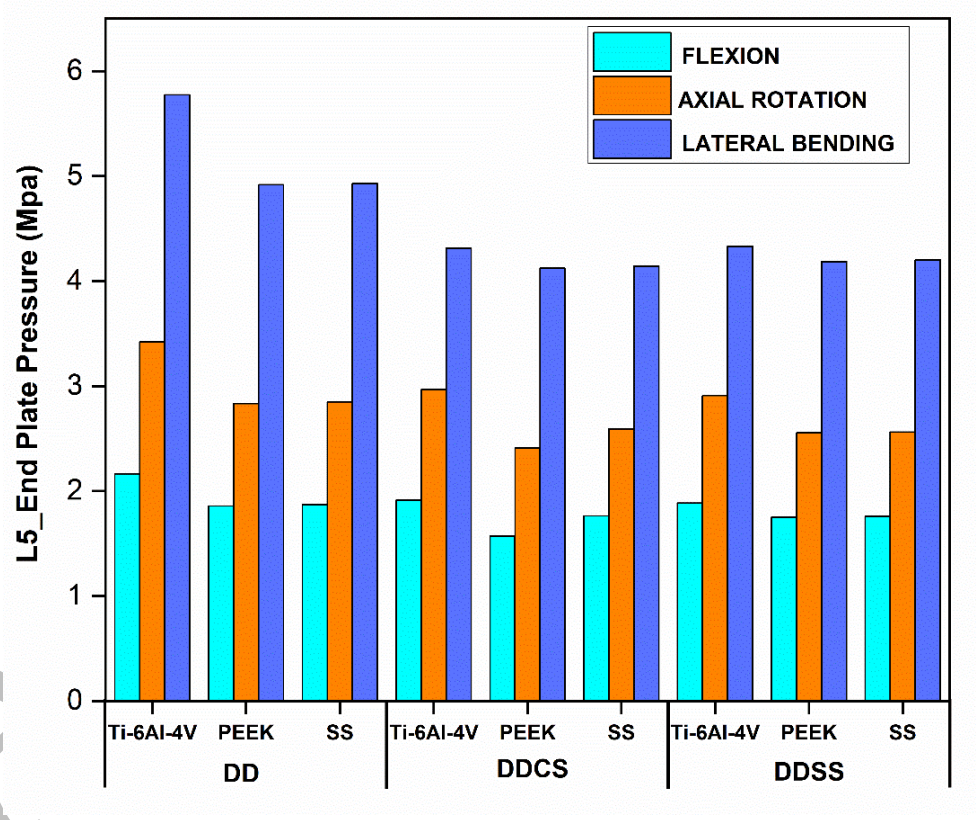

Fig. 18. Graphical representation of von Mises stress on the L5 endplate.

4.5. LIMITATIONS

This study is limited to static analysis due to resource limitation, It will be extended to dynamic analysis in the future. Also, the material assumed as linear property due to simplifying the model for reducing the computational time, but the results are correlated with the literature [24]. This study is limited to the single age group due to the difficulties in the collection of data and the ethical clearance. We agree this limitation may not be suitable for the large group of people study. We assure that it will be useful for the primary study purpose. Also, this study limited unit cell size and lattice structures due to the limitation of computational resources [22]. We will include this limitation in the future. Also, the experimental analysis gives a clear response of implant design. Currently we are considering only numerical analysis is the scope of the work, this is considered for the future extension of work.

5.CONCLUSION

The study analyzed the L4-L5 spine and lattice-structured implants using finite element software, applying force and moment calculations for total deformation and von Misses stress. The maximum deformation of the spine induced by an DD lattice structure PEEK material implant is 0.67 mm under axial rotation motion. The study calculated the VMSS for a lumbar spine implant with three different structures and materials and for two lumbar end plates using various lattice-structured implants under different motions.

The study considered two lumbar endplates and one implant cage for the biomechanical design evaluation. The Von Misses stress of the L4 and L5 end plates and implant cage was extracted. Each part consists of 27 stress plots. The highest Von Mises stress in the Ti-6Al-4V implant is 260.69 MPa (LB with DD), which is less than σ_y (1100 MPa). It clearly shows the Ti-6Al-4V with all lattice structure can withstand the load.

At the same time, the maximum Von Mises stress in PEEK is 282.98 MPa (LB with DD), which does not meet the design criteria of less than σ_y (125 MPa). Likewise, in stainless steel, the maximum von Mises stress is 275.66 MPa (LB with DD), which also meets the design criteria of less than σ_y (290 MPa). It shows that Ti-6Al-4V is suitable for all loading conditions due to its factor of safety. The lowest Von Misses stress in the L4 end plate was 9.24 MPa (flexion with PEEK and DDCS), while the maximum was 19.00 MPa (lateral bending with Ti-6Al-4V and DD).

The lowest Von Misses stress in the L5 end plate was 1.57 MPa (flexion with PEEK and DDCS), while the maximum was 5.77 MPa (lateral bending with Ti-6Al-4V and DD). The study further indicates that the DDCS structure exhibits the lowest stress levels among the tested lattice structures. In conclusion, the DDCS lattice structure combined with Ti-6Al-4V material emerges as the optimal choice for lumbar implants, highlighting its potential as a highly favorable option.

Acknowledgement

We express our gratitude to everybody who supported our research and assisted to resolving the challenges. We did not secure any funding for this research.

Declaration of conflicting interests

All authors declare no competing interests.

REFERENCES

[1] Ayturk U.M., Puttlitz C.M., Parametric convergence sensitivity and validation of a finite element model of the human lumbar spine, Comput Methods Biomech Biomed Engin, 2011, 14(8), 695-705, DOI: 10.1080/10255842.2010.493517.

[2] Cai X.Y., Sun M.S., Huang Y.P., Liu Z.X., Liu C.J., Du C.F., Yang Q., Biomechanical Effect of L4 -L5 Intervertebral Disc Degeneration on the Lower Lumbar Spine: A Finite Element Study, Orthop Surg, 2020, 12(3), 917-930, DOI: 10.1111/os.12703.

[3] Chen C.S., Cheng C.K., Liu C.L., Lo W.H., Stress analysis of the disc adjacent to interbody fusion in lumbar spine, Med Eng Phys, 2001, 23(7), 483-91, DOI: 10.1016/s1350-4533(01)00076-5.

[4] Chen S.H., Lin S.C., Tsai W.C., Wang C.W., Chao S.H., Biomechanical comparison of unilateral and bilateral pedicle screws fixation for transforaminal lumbar interbody fusion after decompressive surgery--a finite element analysis, BMC Musculoskeletal Discord, 2012, 13, DOI: 10.1186/1471-2474-13-72.

[5] Dreischarf M., Zander T., Shirazi-Adl A., Puttlitz C.M., Adam C.J., Chen C.S., Goel V.K., Kiapour A., Kim Y.H., Labus K.M., Little J.P., Park W.M., Wang Y.H., Wilke H.J., Rohlmann A., Schmidt H., Comparison of eight published static finite element models of the intact

lumbar spine: predictive power of models improves when combined together, J Biomech, 2014, 47(8), 1757-66, DOI: 10.1016/j.jbiomech.2014.04.002.

[6] Elkhoury K., Morsink M., Sanchez-Gonzalez L., Kahn C., Tamayol A., Arab-Tehrany E., Biofabrication of natural hydrogels for cardiac, neural, and bone Tissue engineering Applications, Bioact Mater, 2021, 6(11), 3904-3923, DOI: 10.1016/j.bioactmat.2021.03.040.

[7] Fan W., Guo L.X., A comparison of the influence of three different lumbar interbody fusion approaches on stress in the pedicle screw fixation system: Finite element static and vibration analyses, Int J Numer Method Biomed Eng, 2019, 35(3), E3162, DOI: 10.1002/cnm.3162.

[8] Fan Y., Zhou S., Xie T., Yu Z., Han X., Zhu L., Topping-off surgery vs posterior lumbar interbody fusion for degenerative lumbar disease: a finite element analysis, J Orthop Surg Res, 2019, 14(1), DOI: 10.1186/s13018-019-1503-4.

[9] Gould S.L., Cristofolini L., Davico G., Viceconti M., Computational modelling of the scoliotic spine: A literature review, Int J Numer Method Biomed Eng, 2021, 37(10), E3503, DOI: 10.1002/cnm.3503.

[10] Guo L.X., Li R., Zhang M., Biomechanical and fluid flowing characteristics of intervertebral disc of lumbar spine predicted by poroelastic finite element method, Acta of Bioengineering and Biomechanics, 2016, 18(2), 19-29, DOI: 10.5277/ABB-00406-2015-02.

[11] Guo L.X., Teo E.C., Lee K.K., Zhang Q.H., Vibration characteristics of the human spine under axial cyclic loads: effect of frequency and damping, Spine (Phila Pa 1976), 2005, 30(6), DOI: 10.1097/01.brs.0000155409.11832.02.

[12] Hao S., Wang M., Yin Z., Jing Y., Bai L., Su J., Microenvironment-targeted strategy steers advanced bone regeneration, Mater Today Bio, 2023, 22, DOI: 10.1016/j.mtbio.2023.100741.

[13] Johnson J.W., Gadomski B., Labus K., Stewart H., Nelson B., Seim H., Regan D., Von Stade D., Kelly C., Horne P., Gall K., Easley J., Novel 3D printed lattice structure titanium cages evaluated in an ovine model of interbody fusion, JOR Spine, 2023, 6(3), E1268, DOI: 10.1002/jsp2.1268.

[14] Kirnaz S., Capadona C., Lintz M., Kim B., Yerden R., Goldberg J.L., Medary B., Sommer F., Mcgrath L.B., Bonassar L.J., Härtl R., Pathomechanism and Biomechanics of Degenerative Disc Disease: Features of Healthy and Degenerated Discs, Int J Spine Surg, 2021, 15, 10-25, DOI: 10.14444/8052.

[15] Lai Y.P., Lin Y.H., Wu Y.C., Shih C.M., Chen K.H., Lee C.H., Pan C.C., Robot-Assisted Pedicle Screw Placement Led to Lower Screw Loosening Rate than Fluoroscopy-Guided Technique in Transforaminal Lumbar Interbody Fusion for Lumbar Degenerative Disease: A Single-Center Retrospective Study, J Clin Med, 2022, 11(17), DOI: 10.3390/jcm11174989.

[16] Liu C., Guo C., Meng F., Zhu Z., Xia W., Liu H., Perioperative risk factors related to complications of lumbar spine fusion surgery in elderly patients, BMC Musculoskeletal Disord, 2023, 24(1), DOI: 10.1186/s12891-023-06689-z.

[17] Liu Shunyu., Shin Yung., Additive manufacturing of Ti6Al4V alloy: A review, Materials and Design, 2018, 164, DOI: 10.1016/j.matdes.2018.107552.

[18] Lu T., Lu Y., Interlaminar stabilization offers greater biomechanical advantage compared to interspinous stabilization after lumbar decompression: a finite element analysis, J Orthop Surg Res, 2020, 15, DOI: 10.1186/s13018-020-01812-5.

[19] Meganathan S., Alphin M.S., Biomechanical assessment of lumbar stability: finite element analysis of TLIF with a novel combination of coflex and pedicle screws, Acta Bioeng Biomech, 2024, 25(4), 133-143, DOI: 10.37190/abb-02380-2024-04.

[20] Molinari L., Falcinelli C., Gizzi A., Di Martino A., Effect of pedicle screw angles on the fracture risk of the human vertebra: A patient-specific computational model, J Mech Behav Biomed Mater, 2021, 116, DOI: 10.1016/j.jmbbm.2021.104359.

[21] Nakhli Z., Ben Hatira F., Pithioux M., Chabrand P., Saanouni K., On prediction of the compressive strength and failure patterns of human vertebrae using a quasi-brittle continuum damage finite element model, Acta Bioeng. Biomech., 2019, 21(2), 143–151, DOI: 10.5277/ABB-01265-2019-03.

[22] Nongthombam C., Patani S., Gulve N.D., Nehete A., Pardeshi M.P., Aher S., Stress Evaluation of Titanium-gold and Titanium-aluminum-vanadium Alloy for Orthodontic Implants: A

Comparative Finite Element Model Study, J. Indian Orthod. Soc, 2017, 51(4), 245–249, DOI: 10.4103/jios.jios_20_17.

[23] Park W.M., Kim K., Kim Y.H., Effects of degenerated intervertebral discs on intersegmental rotations, intradiscal pressures, and facet joint forces of the whole lumbar spine, Comput Biol Med, 2013, 43(9), 1234-40, DOI: 10.1016/j.compbiomed.2013.06.011.

[24] Ponnappan R.K., Serhan H., Zarda B., Patel R., Albert T., Vaccaro A.R., Biomechanical evaluation and comparison of polyetheretherketone rod system to traditional titanium rod fixation, Spine J, 2009, 9(3), DOI: 10.1016/j.spinee.2008.08.002.

[25] Rohlmann A., Neller S., Claes L., Bergmann G., Wilke H.J., Influence of a follower load on intradiscal pressure and intersegmental rotation of the lumbar spine, Spine (Phila Pa 1976), 2001, 26(24), E557-61, DOI: 10.1097/00007632-200112150-00014.

[26] Ruggeri M., Bianchi E., Rossi S., Vigani B., Bonferoni M.C., Caramella C., Sandri G., Ferrari F., Nanotechnology-Based Medical Devices for the Treatment of Chronic Skin Lesions:From Research to the Clinic, Pharmaceutics, 2020, 12(9), DOI: 10.3390/pharmaceutics12090815.

[27] Samanta A., Lufkin T., Kraus P., Intervertebral disc degeneration-Current therapeutic options and challenges, Front Public Health, 2023, 11, DOI: 10.3389/fpubh.2023.1156749.

[28] Schmidt H., Galbusera F., Rohlmann A., Shirazi-Adl A., What have we learned from finite element model studies of lumbar intervertebral discs in the past four decades, J Biomech, 2013, 46(14), 2342-55, DOI: 10.1016/j.jbiomech.2013.07.014.

[29] Steinmann M., Lampe D., Grosser J., Schmidt J., Hohoff M.L., Fischer A., Greiner W., Risk factors for herpes zoster infections: a systematic review and meta-analysis unveiling common trends and heterogeneity patterns, Infection, 2024, 52(3), 1009-1026, DOI: 10.1007/s15010-023-02156-y.

[30] Tan L.A., Yerneni K., Tuchman A., Li X.J., Cerpa M., Lehman R.A., Lenke L.G., Utilization of the 3D-printed spine model for freehand pedicle screw placement in complex spinal deformity correction, J Spine Surg, 2018, 4(2), 319-327, DOI: 10.21037/jss.2018.05.16.

[31] Teo E.C., Ng H.W., Evaluation of the role of ligaments, facets and disc nucleus in lower cervical spine under compression and sagittal moments using finite element method, Med. Eng. Phys, 2001, 23(3), 155–164, DOI: 10.1016/S1350-4533(01)00036-4.

[32] Tredan D.A., Mobbs R.J., Maharaj M., Parr W.C.H., Combining Virtual Surgical Planning and Patient-Specific 3D-Printing as a Solution to Complex Spinal Revision Surgery, J Pers Med, 2022, 13(1), DOI: 10.3390/jpm13010019.

[33] Urban J.P., Roberts S., Degeneration of the intervertebral disc, Arthritis Res Ther, 2003, 5(3), 120-30, DOI: 10.1186/ar629.

[34] Vallejo R., Gupta A., Cedeno D.L., Vallejo A., Smith W.J., Thomas S.M., Benyamin R., Kaye A.D., Manchikanti L., Clinical Effectiveness and Mechanism of Action of Spinal Cord Stimulation for Treating Chronic Low Back and Lower Extremity Pain: a Systematic Review, Curr Pain Headache Rep, 2020, 24(11), DOI: 10.1007/s11916-020-00907-2.

[35] Walsh W.R., Evans R.O., Iliopoulos J., Cornwall G.B., Thomas K.A., Evaluation of a bioresorbable polylactide sheet for the reduction of pelvic soft tissue attachments in a porcine animal model. Journal of biomedical materials research. Part B, Applied biomaterials, 2006, 79(1), 166-75, DOI: 10.1002/jbm.b.30527.

[36] Wang B., Hua W., Ke W., Lu S., Li X., Zeng X., Yang C., Biomechanical Evaluation of Transforaminal Lumbar Interbody Fusion and Oblique Lumbar Interbody Fusion on the Adjacent Segment: A Finite Element Analysis, World Neurosurg, 2019, 126, e819-e824, DOI: 10.1016/j.wneu.2019.02.164.

[37] Wang Z., And B., Zhang., Weakly solvating electrolytes for next-generation lithium batteries: design principles and recent advances, Energy Mater. Devices, 2023, 1(1), DOI: 10.26599/emd.2023.9370003.

[38] Yang Y., Jiang Y., Qian D., Wang Z., Xiao L., Prevention and treatment of osteoporosis with natural products: Regulatory mechanism based on cell ferroptosis, J Orthop Surg Res, 2023, 18(1), DOI: 10.1186/s13018-023-04448-3.

[39] Zhai W.J., Liu L., Gao Y.H., Qin S.L., Han P.F., Xu Yf., Application of 3D printed porous titanium interbody fusion cage vs. polyether ether ketone interbody fusion cage in anterior

cervical discectomy and fusion: A systematic review and meta-analysis update. Exp Ther Med, 2024, 28(1), DOI: 10.3892/etm.2024.12579.

[40] Zhu J., Shen H., Cui Y., Fogel G.R., Liao Z., Liu W., Biomechanical Evaluation of Transforaminal Lumbar Interbody Fusion with Coflex-F and Pedicle Screw Fixation: Finite Element Analysis of Static and Vibration Conditions, Orthop Surg, 2022, 14(9), 2339-2349, DOI: 10.1111/os.13425.

[41] Zhu S., Dong R., Liu Z., Liu H., Lu Z., Guo Y., A finite element method study of the effect of vibration on the dynamic biomechanical response of the lumbar spine, Clin Biomech (Bristol, Avon), 2024, 111, DOI: 10.1016/j.clinbiomech.2023.106164.